



OPEN

Origin of the enhanced Nb₃Sn performance by combined Hf and Ta doping

Chiara Tarantini¹✉, Fumitake Kametani^{1,2}, Shreyas Balachandran¹, Steve M. Heald³, Laura Wheatley⁴, Chris R. M. Grovenor⁴, Michael P. Moody⁴, Yi-Feng Su^{1,5}, Peter J. Lee¹ & David C. Larbalestier^{1,2}

In recent years there has been an increasing effort in improving the performance of Nb₃Sn for high-field applications, in particular for the fabrication of conductors suitable for the realization of the Future Circular Collider (FCC) at CERN. This challenging task has led to the investigation of new routes to advance the high-field pinning properties, the irreversibility and the upper critical fields (H_{irr} and H_{c2} , respectively). The effect of hafnium addition to the standard Nb-4Ta alloy has been recently demonstrated to be particularly promising and, in this paper, we investigate the origins of the observed improvements of the superconducting properties. Electron microscopy, Extended X-ray Absorption Fine Structure Spectroscopy (EXAFS) and Atom Probe Tomography (APT) characterization clearly show that, in presence of oxygen, both fine Nb₃Sn grains and HfO₂ nanoparticles form. Although EXAFS is unable to detect significant amounts of Hf in the A15 structure, APT does indeed reveal some residual intragrain metallic Hf. To investigate the layer properties in more detail, we created a microbridge from a thin lamella extracted by Focused Ion Beam (FIB) and measured the transport properties of Ta-Hf-doped Nb₃Sn. $H_{c2}(0)$ is enhanced to 30.8 T by the introduction of Hf, ~1 T higher than those of only Ta-doped Nb₃Sn, and, even more importantly the position of the pinning force maximum exceeds 6 T, against the typical ~4.5–4.7 T of the only Ta-doped material. These results show that the improvements generated by Hf addition can significantly enhance the high-field performance, bringing Nb₃Sn closer to the requirements necessary for FCC realization.

Nb₃Sn is being used to advance beyond Nb-Ti for the High Luminosity upgrade of the Large Hadron Collider ongoing at CERN, and it will be essential for the construction of the Future Circular Collider (FCC) in order to reduce or eliminate the cost of using High Temperature Superconductors (HTS)^{1,2}. However, the FCC requirements in terms of non-Cu critical current density (non-Cu $J_c > 1500$ A/mm² at 16 T and 4.2 K), residual resistivity ratio of the Cu stabilized (conductor RRR > 150 to maintain > 100 after cabling and winding) and filament diameter ($d_{eff} < 20$ μm) are very challenging and beyond the performance of presently available commercial Nb₃Sn wires^{3,4}. For this reason in the last few years there has been an increasing effort to improve the J_c performance of internal-tin (IT) and powder-in-tube (PIT) wires by investigating the phase evolution and by heat treatment optimizations^{5–9}. Although a 36% J_c increase ($J_c(4.2$ K, 16 T) ~ 1300 A/mm²) was achieved in small filament diameter RRP (Restacked Rod Process) wires⁸, other approaches have also been pursued. The most promising is the introduction of artificial pinning centres by internal oxidation of the Nb alloy to form oxide nanoparticles, a technique which was first developed at GE (General Electric) in 1994 using Nb-Zr to form ZrO₂^{10,11}, and which was recently re-examined using SnO₂ as oxygen source^{12,13}. Despite a clear shift to higher field of the pinning force maximum caused by the introduced pinning centres, adding only Zr causes a suppression of the irreversibility field H_{irr} (and upper critical field H_{c2}), clearly an undesirable feature for a high-field superconductor. In order to overcome this limitation, ternary alloys, such as Nb₄Ta₁Zr and Nb₄Ta₁Hf (atomic %) were developed to combine both the H_{c2} enhancing property of Ta with the pinning enhancing feature of Zr or Hf oxide nanoparticles¹⁴ (a similar study was conducted at the same time using NbTaZr alloy¹⁵). Although Hf had been previously used for Nb₃Sn¹⁶, it had never been combined with Ta or with oxides. Our wires were made with

¹National High Magnetic Field Laboratory, Florida State University, Tallahassee, FL 32310, USA. ²Department of Mechanical Engineering, FAMU-FSU College of Engineering, Florida State University, Tallahassee, FL 32310, USA. ³Advanced Photon Source, Argonne National Laboratory, Argonne, IL 60439, USA. ⁴Department of Materials, Oxford University, Parks Road, Oxford OX1 3PH, UK. ⁵Now at Materials Science and Technology Division, Oak Ridge National Laboratory, Oak Ridge, TN 37831, USA. ✉email: tarantini@asc.magnet.fsu.edu

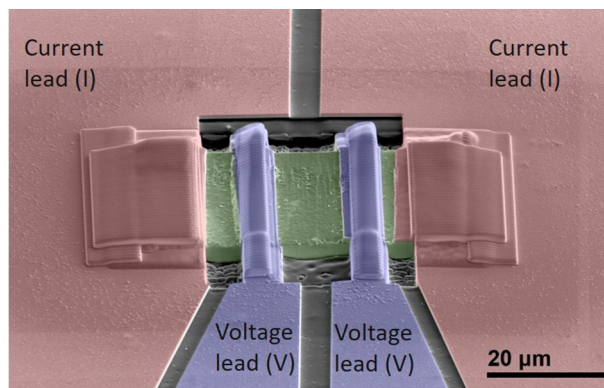


Figure 1. SEM image of Ta-Hf-doped Nb₃Sn microbridge. False-coloured SEM image of a thin lamella (green) extracted by focused ion beam (FIB) from a Ta-Hf-doped Nb₃Sn sample. The FIB'ed lamella is mounted on a MgO substrate. The current (pink) and voltage (blue) leads for transport measurements were deposited using a Gas Injection System (GIS).

a Nb-alloy rod surrounded by Cu-Sn powders (either with or without additional SnO₂) introduced into Ta/Cu tubes. The best A15 performance was obtained with the Nb₄Ta₁Hf alloy with similar J_c and pinning properties either with or without SnO₂. The pinning force (F_p) maximum, H_{Max} , evaluated by magnetic characterizations was observed at ~ 5.8 T in the TaHf-Nb₃Sn sample, significantly higher than in Ta-Nb₃Sn, where typically H_{Max} is at ~ 4.6 T. Moreover, the magnetization-estimated layer J_c (16 T) reached 3700 A/mm² which, translated to a typical RRP layout, would lead to a non-Cu J_c of 2230 A/mm², about 50% higher than the FCC specifications. Because of the wire design, transport measurements could not be directly performed on these samples and no H_{c2} characterization was carried out.

To better understand the origin of the enhanced pinning performance, in this study we directly investigated the superconducting properties of TaHf-Nb₃Sn sample heat-treated at 550 °C/100 h + 670 °C/100 h by in-field transport measurements of the resistive transition to determine $H_{c2}(T)$, $H_{irr}(T)$ and the field dependence of the pinning force $F_p(H)$. FESEM (field emission scanning electron microscopy) microstructure characterization was performed on fractured TaHf-Nb₃Sn samples after different heat treatments and on a commercial Ta-doped RRP wire to compare the grain sizes. Extended X-ray Absorption Fine Structure Spectroscopy (EXAFS) characterization was carried out to evaluate where the Ta and Hf dopants are located in the Nb₃Sn structure, whereas Atom Probe Tomography (APT) was used to provide local chemical composition, identifying also segregants and/or particles.

Results

To overcome the limitation of the inductive characterization in our earlier evaluation of the superconducting properties, a microbridge for transport measurements was fabricated from the A15 layer of the wire heat treated at 670 °C. This microbridge allowed us to directly investigate the effect of the Hf addition on H_{c2} and to verify the shift towards high field of the F_p maximum. To fabricate the microbridge (shown in Fig. 1), a thin A15 lamella was sculpted out by Focused Ion Beam (FIB) and mounted on a MgO substrate. Metal current and voltage leads were then deposited by Gas Injection System (GIS) in the FIB. Some Ga ion implantation is expected during FIB bombardment (30 kV), producing a thin amorphous layer at the sample surface and with a maximum Ga penetration of the order of few tens of nm. This low level of Ga should not impact the superconducting properties of the sample (see “Methods”). The effective cross-sectional area of the Nb₃Sn lamella could not be accurately measured: in fact, because of the brittle nature of the A15 phase, microfractures could easily be introduced when the FIB'ed lamella was extracted from the rest of the sample by the ex-situ micromanipulator. Although these types of damage did not prevent transport characterizations, they did prevent the evaluation of resistivity and J_c of the microbridge. Therefore, the transport characterizations were performed in 16 T QD-PPMS (equipped with external instruments) to obtain $R(T,H)$ curves and to determine H_{c2} and H_{irr} . The resistive data, reported in Fig. 2a, show a very low noise level of few nV, corresponding to the intrinsic limit of our set-up, indicative of the high quality of microbridge and contacts. The transitions remained very sharp with almost no broadening when high field was applied, confirming the homogeneity of the sample. The curves were analysed with different resistive criteria, as shown in Fig. 2b, to estimate H_{c2} (typically estimated at 99 or 90 of the normal state resistance, R_N ; sometime at 50%) and H_{irr} (typically estimated at 10 or 1% of R_N). All datasets were fitted with the dirty-limit Werthamer, Helfand, and Hohenberg (WHH) model¹⁷ in order to estimate the zero-temperature values. Despite a slightly suppressed T_c , H_{c2} in this Ta-Hf-doped wire is higher than that measured in only Ta-doped samples. In fact, in a wide high-field characterization campaign on Ta-doped Nb₃Sn samples Godeke et al.¹⁸ estimated in a similarly heat treated sample (675 °C/64 h) a $\mu_0 H_{c2,99\%}(0) \sim 29.7$ T, whereas in our TaHf-sample we found $\mu_0 H_{c2,99\%}(0) \sim 30.8$ T, 1.1 T higher than in the Ta-case.

Despite the uncertainty in the lamella cross-section and the small surface area of the contacts in this microbridge, we were able to perform I-V characterizations and to investigate the profile of pinning force curves at different temperature between 4.2 and 15 K and up to 16 T (Fig. 2c). These data show that F_p maximum, H_{max}

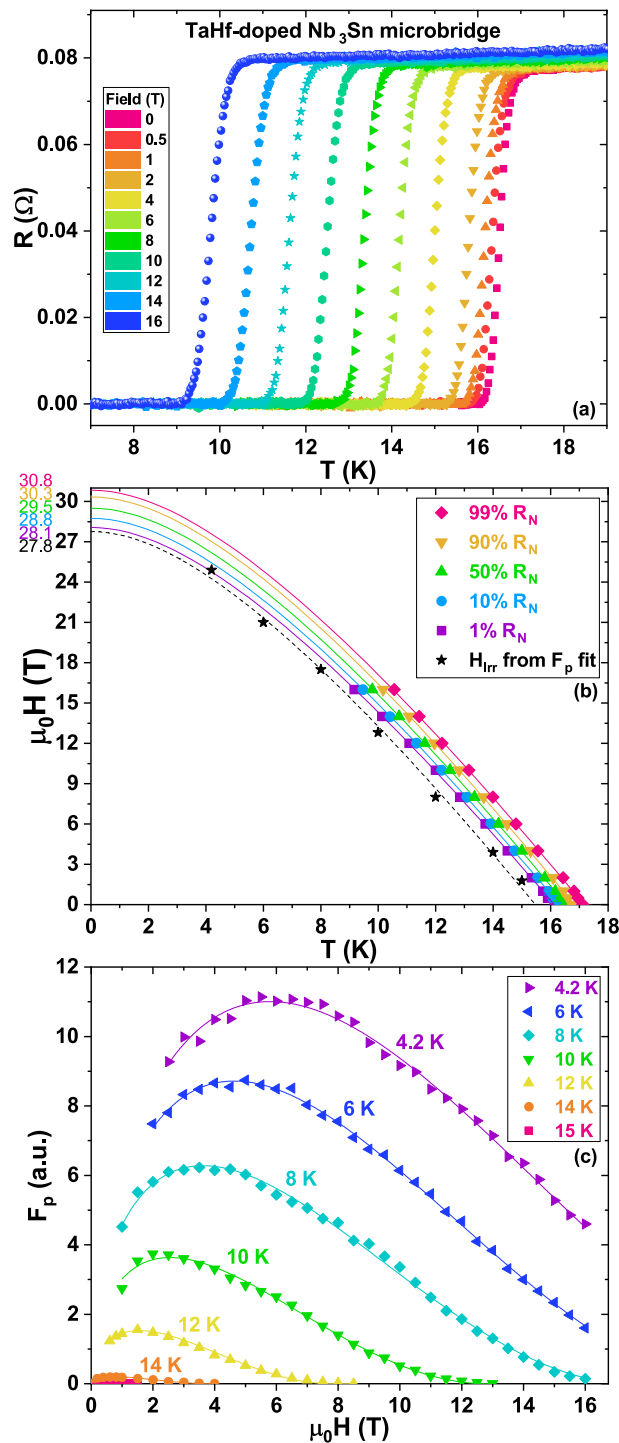


Figure 2. Transport characterizations of Ta-Hf-doped Nb₃Sn microbridge. Superconducting characterization of a Ta-Hf doped Nb₃Sn sample. (a) Resistive transitions at field up to 16 T. (b) H_{c2} (H_{irr}) versus temperature determined by different resistive criteria (see text) from (a) and from the fits in (c). (c) F_p versus field data at different temperatures with fitting curves (see text).

at 4.2 K is at about 6 T (the value estimated by magnetization was of 5.8 T)¹⁴, confirming the shift towards higher field with respect of typical Ta-doped value (~ 4.6 – 4.7 T). All $F_p(H)$ curves in Fig. 2c are well reproduced taking into account two pinning mechanisms, by grain boundaries (GB) and point defects (PD)¹⁹, using the equation $F_p(H) = A_{GB}f_{GB}\left(\frac{H}{H_{irr}}\right) + A_{PD}f_{PD}\left(\frac{H}{H_{irr}}\right) = a_{GB}f_{GB, norm}f_{GB}\left(\frac{H}{H_{irr}}\right) + a_{PD}f_{PD, norm}f_{PD}\left(\frac{H}{H_{irr}}\right)$, where $f_{GB}(h) = h^{0.5}(1-h)^2$ and $f_{PD}(h) = h(1-h)^2$ ($f_{GB, norm}$ and $f_{PD, norm}$ are the factors normalizing f_{GB} and f_{PD} to their maxima). Insulating oxide nanoparticles are a typical provider of point defect pinning sites. At 4.2 K the

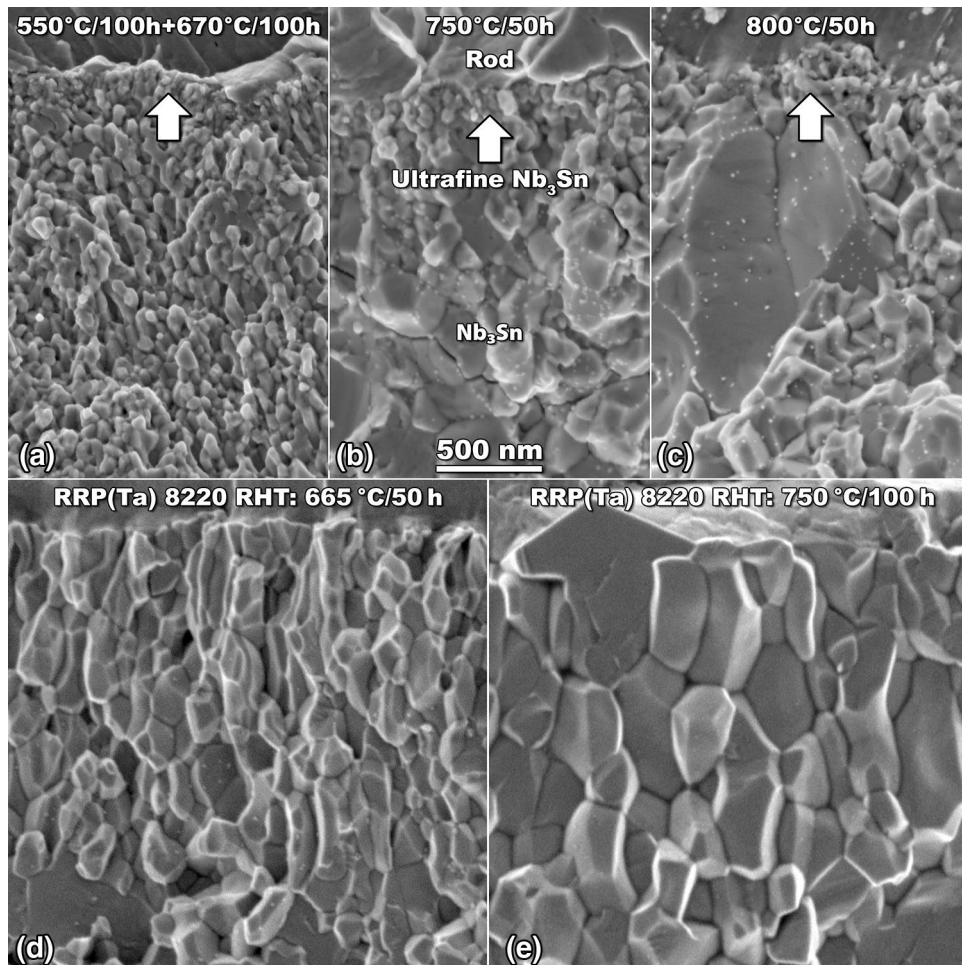


Figure 3. SEM characterization of Ta-Hf-doped Nb_3Sn compared with standard Ta-doped Nb_3Sn . Fractographs of Nb_3Sn grains after heat treatments at different temperature for Ta-Hf-doped samples made with home-made $\text{Nb}_4\text{Ta}_1\text{Hf}$ special alloy (a–c) and for Ta-doped RRP wire made with industrial Nb_4Ta (d,e).

PD contribution is significant with $A_{PD} \sim 0.57A_{GB}$ ($a_{PD} \sim 0.3a_{GB}$), but it is sharply suppressed with increasing temperature, becoming negligible at 10 K. Since the pinning efficiency is maximized when the defect sizes are about twice the coherence length, this loss of point pinning efficiency with increasing temperature suggests that a dimensional cross-over occurs at about 10 K, leaving only the grain boundaries as effective pinning centres at higher temperature. The $F_p(H)$ curve fits allow an estimation of the H_{irr} values, shown in Fig. 2b. As for the H_{c2} data, they are fitted using the WHH model: the estimated $H_{irr}(0)$ is 27.8 T, close to the value estimated from the $R(T,H)$ measurements.

To understand the microstructural origin of the high field shift of H_{max} , we used fractographs of the Nb_3Sn layer for the Ta-Hf-doped wire reacted at 670 °C. Figure 3a reveals very small grains, with an average size of less than 70 nm, produced in a thick A15 layer (typical grain size in Ta-only doped Nb_3Sn is 100–150 nm)²⁰. However, no obvious particle or defect was observed that could explain the origin of the point defects. To investigate the evolution of the Nb_3Sn microstructure in presence of both Ta and Hf, we also performed very high temperature heat treatments at 750 and 800 °C. Such high temperature heat treatments are, in general, undesirable because they are more difficult to use for wind-and-react magnets and because they cause grain growth, which is detrimental for the pinning performance. However, in this case the grain growth can be useful because it allows us to compare the difference in Nb_3Sn grain growth depending on the dopants and to identify nanoparticles. Figure 3b,c show additional fractographs at 750 and 800 °C for the Ta-Hf-doped A15 layer compared with the typical microstructures in Fig. 3d,e of a RRP wire made with standard Nb_4Ta alloy and reacted at 665 and 750 °C, respectively. Although the Ta-Hf-doped Nb_3Sn grains grow with increasing HT temperature up to 800 °C (Fig. 3b,c), their sizes are still limited and very fine grains are still present near the unreacted alloy rod as a result of the delayed recrystallization of the Nb-4Ta-1Hf alloy compared with Nb-4Ta^{14,21}. In fact, Fig. 3d,e shows the much larger A15 grains obtained in a Ta-doped A15 after the 665 and 750 °C reactions. Another important finding is that, although it is not possible to distinguish HfO_2 nanoparticles in the 670 °C case, where the A15 grains are extremely small, they are obvious after the 750–800 °C HTs of the Ta-Hf wire, where the nanoparticles are clearly visible decorating the exposed grain boundaries. This result and the presence of a significant point

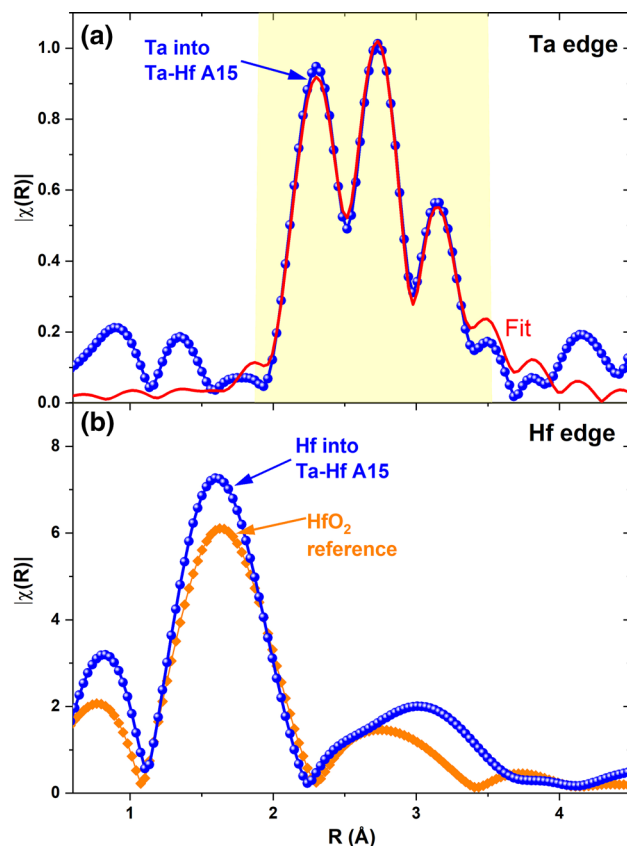


Figure 4. EXAFS characterization of Ta-Hf-doped sample. Fourier transforms of the k^2 weighted $\chi(k)$ data for the (a) Ta L_3 and (b) Hf L_3 edges of the EXAFS characterizations of the Ta-Hf-doped Nb_3Sn sample heat treated at 670°C (blue dots) and of the reference HfO_2 sample (orange diamond). In (a) the red line is the two-site fit for the Nb_3Sn structure (fitting window of interest for Nb_3Sn from 1.9 to 3.5 Å).

pinning contribution in the F_p analysis suggests that the nanoparticles are also present after the 670°C HT but that they are too small or too similar in size to the A15 facets to be distinguished.

To clarify the nature of the point defects affecting the low-temperature pinning performance and to understand which role the two dopants play in the Nb_3Sn layer, we also investigated our $\text{Nb}_4\text{Ta}_1\text{Hf}$ -alloyed Nb_3Sn sample using EXAFS. This technique allows us to determine whether a specific element is substituting for Nb and/or for Sn in the A15 structure or is located in another structure. In this case we focused our study on the EXAFS signals for both the Ta and the Hf edges produced by the A15 layer. The Fourier transform of the Ta-edge spectrum (Fig. 4a) reveals the typical 3-peak structure of the A15 phase due to majority Ta occupancy of the Nb sites (the three peaks are due to the three nearby coordination shells for the Nb site; occupancy of only the Sn site would produce one single peak in the central position)²². In fact, fitting these data shows that only a minor amount of Ta, $\sim 12\%$, sits on the Sn site. Interestingly, this level of split site occupancy for Ta is compatible with that found for the Ta-doped RRP wire after similar heat-treatment²³, suggesting that the presence of Hf does not affect the Ta occupancy behaviour. A similar analysis of the A15 layer for the Hf edge shows no clear indication of Hf being in the A15 structure (Fig. 4b): in fact, the major peak does not correspond to any of the peaks for the A15 phase, either the Nb or Sn site (compare with Fig. 4a). On the contrary, the Fourier transform of the spectrum obtained on the Ta-Hf-doped A15 layer corresponds to that obtained on the Hf edge of a reference HfO_2 sample, suggesting that the Hf present in the Nb_3Sn is mostly oxidized. It is important to note that, because of the proximity of the Hf edge to the Ta edge (they differ by ~ 320 eV), a quantitative analysis of the EXAFS signal of Hf cannot be performed, limiting our analysis to the qualitative description given above (see Supplementary Information and Figure S1 for details). Since the Fourier transform in Fig. 4b is dominated by the HfO_2 signal, the presence of Hf in the A15 phase at levels obscured by the HfO_2 component cannot be excluded by EXAFS.

To explore the possibility that very small HfO_2 particles exist in the 670°C sample, we employed Atom Probe Tomography analysis. This requires FIB'ing a needle-shaped sample out of the A15 layer²⁴, and accelerating the atoms from the sample toward a detector²⁵. Figure 5 shows a typical APT reconstruction of a volume of material containing several A15 grains. Copper is known to segregate to the GBs of Nb_3Sn ^{26,27} and so the 4 at% Cu iso-concentration surfaces reveal the location of the GBs (orange surfaces). We can identify separate peaks from metallic (unoxidized) Hf species and from HfO molecular ions in the mass spectra, and the distribution of these species is very different. The locations of HfO_2 nanoparticles are clearly identified by the 1.5 ionic% iso-concentration surfaces for HfO species in Fig. 5 (blue surfaces in the left image), and their average diameter is ~ 3 nm with a density of $\sim 5 \times 10^{22}$ particles/ m^3 . Clearly these HfO_2 nanoparticles are not preferentially

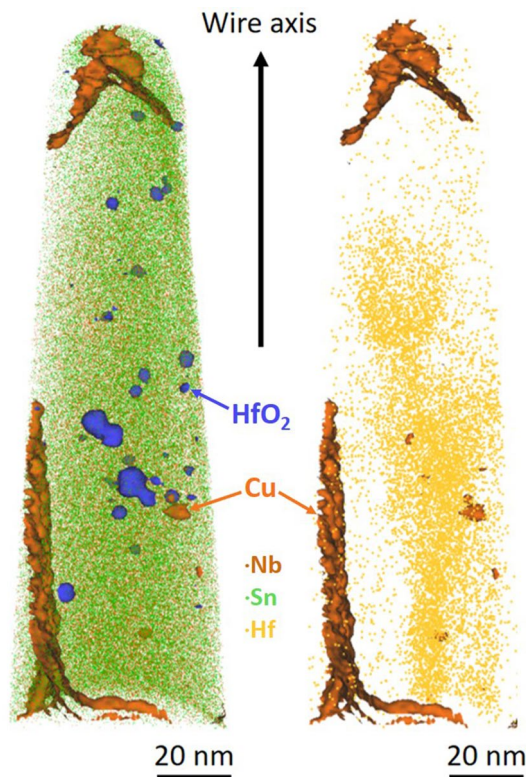


Figure 5. Atom Probe Tomography of Ta-Hf-doped Nb₃Sn sample. Atom Probe Tomography of a needle-shaped sample (tip at the top of the figure) extracted by FIB from the A15 layer of the Ta-Hf doped Nb₃Sn wire. The 4 at% copper iso-concentration surfaces in orange, identify the grain boundaries (and a few nanoparticles in the A15 grains). The blue iso-surfaces at 1.5 ionic% of HfO molecular species, in the left-hand image, identify the HfO nanoparticles; brown and green dots are Nb and Sn, respectively. In the right-hand image, the un-oxidized Hf species are represented by yellow spots.

segregated at GBs but are found inside the A15 grain interiors. The right image of Fig. 5 shows the distribution of the un-oxidized Hf species, again within the A15 grains, but neither in the HfO₂ particles nor in independent clusters. The combined EXAFS and APT results imply that, although the HfO₂ nanoparticles are not clearly identifiable in the fractography of the sample heat treated at 670 °C (they are too small and fractography exposes only the GB interfaces), they are indeed present and likely the origin of the point-defect pinning contribution. The APT data also suggests that at least some of the Hf is not oxidized but is present as the solid solution in the A15 grains, although it gives no information on what site they occupy. The intragrain Hf concentration is estimated to be less than 0.1 at%, a small amount unlikely to be detectable by EXAFS.

Discussion and conclusions

In this paper we investigated the origin of the enhanced performance of Nb₃Sn made with a recently developed Nb₄Ta₁Hf alloy. The superconducting properties were measured in transport on a FIB-sculpted microbridge. They revealed an upper critical field H_{c2} that is about 1 T higher than the typical values obtained on standard Nb₄Ta-alloyed Nb₃Sn wires and can be attributable to the introduction of Hf. Furthermore, we observe a significant shift toward high field of the pinning force F_p maximum (~ 6 T versus 4.6–4.7 T in Ta-doped A15 samples). Deconvolution of the $F_p(H)$ curves clearly indicate a change in the pinning mechanisms, with a nanoparticle contribution being added to the typical grain-boundary pinning mechanism. Since this type of pinning mechanism is typically caused by the presence of point defects, such as nanoparticles, we investigated the microstructure by SEM imaging of fracture surfaces, and found that the A15 grains were significantly smaller than in the Ta-only case but we only saw a few nanoparticles. However, nanoparticles were more clearly observed in similarly prepared samples that underwent more extreme heat treatments. To better understand the role and effect of the Hf-addition on the A15 phase and its properties, we performed EXAFS characterizations that can reveal elemental substitution in the crystalline structure. We found that a significant amount of Hf is oxidized but, because of the closeness of the Ta and Hf absorption edges, no quantitative analysis of the presence of small amount of Hf in the A15 structure was possible. EXAFS, however, reveals that the addition of Hf does not affect the substitutional behaviour of Ta in the A15 structure, which is highly desirable because Ta is H_{c2} -enhancing. Finally, we performed Atom Probe Tomography that unequivocally reveals the presence of a high concentration of HfO₂ nanoparticles with an average diameter of about 3 nm, too small to identify with the other techniques, with a density of 5×10^{22} particles/m³. According to ref.¹⁹, the A_{PD}/A_{GB} ratio obtained from the F_p fit can be expressed as $V_{p/}(1.16 \cdot a \cdot S_v)$, where S_v is the GB pinning surface area per unit volume projected in the direction

of the Lorentz force, whereas a is the effective nanoparticle diameter and V_f is the fraction of flux-line lengths inside the nanoparticles. $S_v \approx 1/d$ (with d being the average grain size) and V_f should be between $(a/l)^3$ and (a/l) in case of rigid and flexible flux lines, respectively (l being the average nanoparticle spacing), with V_f typically closer to $(a/l)^3$. Using the microstructural information obtained by SEM (grain size) and APT (nanoparticle diameter and density), A_{pp}/A_{GB} should range from ≈ 0.03 to ≈ 2.2 , which is consistent with our experimental value of 0.57 with rather rigid flux lines.

APT study also shows presence of un-oxidized Hf within the A15 grains. It is presently unclear if this small amount of intragrain Hf, substituted into the A15 structure and presumably increasing the resistivity, is directly responsible for the H_{c2} enhancement or if other indirect factors are playing a role. Because Hf addition decreases the grain size and increases the grain boundary density, the Sn diffusion rate should be enhanced, possibly leading to a more Sn-rich, more homogeneous and better performing A15 phase. Another possibility is that the HfO₂ nanoparticles strain the A15 structure, increasing the electron scattering and consequently H_{c2} .

In conclusion, these findings on the intrinsic properties of Ta-Hf-doped Nb₃Sn are promising from the point of view of the fabrication of conductors with improved high-field properties because of the combined effects of the high H_{c2} and the pinning-enhancing properties produced by the addition of Hf. The challenging task is now to reproduce such properties in a high- J_c /high RRR conductor suitable for accelerator magnets.

Methods

The Ta-Hf-doped Nb₃Sn sample, made with Nb₄Ta₁Hf (atomic %) alloy, was realized as described in ref.¹⁴. The resulting doping levels into the A15 grains, far from the precipitates, were 3 at% of Ta and <0.1 at% of Hf, as estimated by APT analysis. SEM characterization was performed in a Zeiss 1540 EsB Crossbeam Field Emission Scanning Electron Microscope (FESEM) using the in-lens secondary electron detector, whereas the microbridge fabrication were made in a Thermo Fisher Scientific Helios G4 UC FESEM equipped with Focused Ion Beam (FIB). To verify that Ga implantation does not significantly impact our sample properties, we estimated the depth of Ga penetration by simulation with the widely used Stopping and Range of Ions in Solids (SRIM) software²⁸. We calculated a peak in the Ga concentration at about 10 nm from the surface and no Ga penetrating more than 35–40 nm. Since the thinnest sample dimension is 2.5 μ m, about 99% of the sample cross-section should be Ga-free. Moreover, TEM of similar FIBed samples reveals that Ga is limited to an amorphous layer at the surface that, not having an A15 structure, has no effect of the superconducting properties. A Micro Support Axis Pro SS ex-situ micromanipulator was used for lifting out the FIBed lamella. Pt contacts were deposited using the ion/electron beam induced deposition and gas injection system (GIS) integrated into our FIB/FESEM. Transport characterizations were performed on the microcircuit in a Quantum Design 16 T physical property measurement system (PPMS) in which we used the four-contact measurement technique in maximum Lorentz force configuration. EXAFS characterizations and analysis were performed at the Advanced Photon Source beamline 20-ID at Argonne National Laboratory in conditions similar to those used in ref.²². The measurements were made in fluorescence using a bent Laue detector crystal with ~ 30 eV energy resolution to better separate the Hf and Ta fluorescence signals from the background Cu fluorescence. The x-ray beam size was 2 μ m. See Supplementary Information for more details on EXAFS. Samples for the Atom Probe Tomography (APT) were created in a Zeiss 540 Crossbeam electron microscope using a Zeiss Nvision 40 FIB. The APT analysis was performed at a temperature of 60 K in a LEAP5000-XS in laser mode with a laser energy of 80 pJ.

Received: 10 June 2021; Accepted: 19 August 2021

Published online: 08 September 2021

References

- Ballarino, A. *et al.* The CERN FCC conductor development program: A worldwide effort for the future generation of high-field magnets. *IEEE Trans. Appl. Supercond.* **29**, 6000709 (2019).
- Benedikt, M., Blondel, A., Janot, P., Mangano, M. & Zimmermann, F. Future circular colliders succeeding the LHC. *Nat. Phys.* **16**, 402–407 (2020).
- Ballarino, A. & Bottura, L. Targets for R D on Nb₃Sn conductor for high energy physics. *IEEE Trans. Appl. Supercond.* **25**, 6000906 (2015).
- Tommasini, D. *et al.* The 16 T dipole development program for FCC. *IEEE Trans. Appl. Supercond.* **27**, 4000405 (2017).
- Scheuerlein, C. *et al.* Coarse Nb₃Sn grain formation and phase evolution during the reaction of a high Sn content internal tin strand. *IEEE Trans. Appl. Supercond.* **21**, 2554–2558 (2011).
- Scheuerlein, C., Di Michiel, M., Arnau Izquierdo, G. & Buta, F. Phase transformations during the reaction heat treatment of internal tin Nb₃Sn strands with high Sn content. *IEEE Trans. Appl. Supercond.* **18**, 1754–1760 (2008).
- Pong, I., Oberli, L.-R. & Bottura, L. Cu diffusion in Nb₃Sn internal tin superconductors during heat treatment. *Supercond. Sci. Technol.* **26**, 105002 (2013).
- Sanabria, C. *et al.* Controlling Cu–Sn mixing so as to enable higher critical current densities in RRP* Nb₃Sn wires. *Supercond. Sci. Technol.* **31**, 064001 (2018).
- Segal, C., Tarantini, C., Lee, P. J. & Larbalestier, D. C. Improvement of small to large grain A15 ratio in Nb₃Sn PIT wires by inverted multistage heat treatments. *IOP Conf. Ser. Mater. Sci. Eng.* **279**, 012019 (2017).
- Rumaner, L. E. & Benz, M. G. Effect of oxygen and zirconium on the growth and superconducting properties of Nb₃Sn. *Metall. Mater. Trans. A* **25**, 203–212 (1994).
- Rumaner, L. E., Benz, M. G. & Hall, E. L. The role of oxygen and zirconium in the formation and growth of Nb₃Sn grains. *Metall. Mater. Trans. A* **25**, 213–219 (1994).
- Xu, X., Sumption, M. D. & Peng, X. Internally oxidized Nb₃Sn strands with fine grain size and high critical current density. *Adv. Mater.* **27**, 1346–1350 (2015).
- Motowidlo, L. R. *et al.* An intermetallic powder-in-tube approach to increased flux-pinning in Nb₃Sn by internal oxidation of Zr. *Supercond. Sci. Technol.* **31**, 014002 (2018).

14. Balachandran, S. *et al.* Beneficial influence of Hf and Zr additions to Nb₄at%Ta on the vortex pinning of Nb₃Sn with and without an O source. *Supercond. Sci. Technol.* **32**, 044006 (2019).
15. Xu, X., Rochester, J., Peng, X., Sumption, M. & Tomsic, M. Ternary Nb₃Sn superconductors with artificial pinning centers and high upper critical fields. *Supercond. Sci. Technol.* **32**, 02LT01 (2019).
16. Sekine, H., Takeuchi, T. & Tachikawa, K. Studies on the composite processed Nb-Hf/Cu-Sn-Ga high-field superconductors. *IEEE Trans. Magn.* **17**, 383–386 (1981).
17. Werthamer, N. R., Helfand, E. & Hohenberg, P. C. Temperature and purity dependence of the superconducting critical field, H_{c2} . III. Electron spin and spin-orbit effects. *Phys. Rev.* **147**, 295 (1966).
18. Godeke, A. *et al.* The upper critical field of filamentary Nb₃Sn conductors. *J. Appl. Phys.* **97**, 093909 (2005).
19. Dew-Hughes, D. Flux pinning mechanisms in type II superconductors. *Philos. Mag.* **30**, 293–305 (1974).
20. Tarantini, C., Lee, P. J., Craig, N., Ghosh, A. & Larbalestier, D. C. Examination of the trade-off between intrinsic and extrinsic properties in the optimization of a modern internal tin Nb₃Sn conductor. *Supercond. Sci. Technol.* **27**, 065013 (2014).
21. Balachandran, S. *et al.* *in preparation*.
22. Heald, S. M. *et al.* Evidence from EXAFS for different Ta/Ti site occupancy in high critical current density Nb₃Sn superconductor wires. *Sci. Rep.* **8**, 4798 (2018).
23. Tarantini, C. *et al.* Ta, Ti and Hf effects on Nb₃Sn high-field performance: Temperature-dependent dopant occupancy and failure of Kramer extrapolation. *Supercond. Sci. Technol.* **32**, 124003 (2019).
24. Miller, M. K., Russell, K. F., Thompson, K., Alvis, R. & Larson, D. J. Review of atom probe FIB-based specimen preparation methods. *Microsc. Microanal.* **13**, 428–436 (2007).
25. Miller, M. K. & Forbes, R. G. Atom probe tomography. *Mater. Charact.* **60**, 461–469 (2009).
26. Sandim, M. J. R. *et al.* Grain boundary segregation in a bronze-route Nb₃Sn superconducting wire studied by atom probe tomography. *Supercond. Sci. Technol.* **26**, 055008 (2013).
27. Rodrigues, D., Thieme, C. L. H., Pinatti, D. G. & Foner, S. Grain boundary compositions, transport and flux pinning of multifilamentary Nb₃Sn wires. *IEEE Trans. Appl. Supercond.* **5**, 1607–1610 (1995).
28. Biersack, J. P. & Ziegler, J. F. The stopping and range of ions in solids. In *Ion Implantation Techniques* (eds Ryssel, H. & Glawischnig, H.) 122–156 (Springer, 1982).

Acknowledgements

This work is funded by the US Department of Energy, Office of Science, and Office of High Energy Physics under Award Number DE-SC0012083 and by CERN, and it was performed under the purview of the US-Magnet Development Program. This work was performed at the National High Magnetic Field Laboratory, which is supported by National Science Foundation Cooperative Agreements NSF DMR-1644779 and by the State of Florida. This research used resources of the Advanced Photon Source, an Office of Science User Facility operated for the US Department of Energy (DOE) Office of Science by Argonne National Laboratory, and was supported by the US DOE under Contract No. DE-AC02-06CH11357, and the Canadian Light Source and its funding partners. LW acknowledges support from the Oxford University EPSRC doctoral Training Account.

Author contributions

C.T. performed transport characterizations and analysis and drafted the manuscript. F.K. and Y.S. FIB'ed the sample and prepared the microbridge. S.B. manufactured and heat treat the sample. S.M.H. performed EXAFS characterization. L.W., C.R.M.G. and M.P.M. performed APT analysis. P.J.L. performed FESEM characterization. C.T., S.B., P.J.L. and D.C.L. designed the study. All authors contributed to the manuscript, discussing results and implications.

Competing interests

The authors declare no competing interests.

Additional information

Supplementary Information The online version contains supplementary material available at <https://doi.org/10.1038/s41598-021-97353-w>.

Correspondence and requests for materials should be addressed to C.T.

Reprints and permissions information is available at www.nature.com/reprints.

Publisher's note Springer Nature remains neutral with regard to jurisdictional claims in published maps and institutional affiliations.



Open Access This article is licensed under a Creative Commons Attribution 4.0 International License, which permits use, sharing, adaptation, distribution and reproduction in any medium or format, as long as you give appropriate credit to the original author(s) and the source, provide a link to the Creative Commons licence, and indicate if changes were made. The images or other third party material in this article are included in the article's Creative Commons licence, unless indicated otherwise in a credit line to the material. If material is not included in the article's Creative Commons licence and your intended use is not permitted by statutory regulation or exceeds the permitted use, you will need to obtain permission directly from the copyright holder. To view a copy of this licence, visit <http://creativecommons.org/licenses/by/4.0/>.

© The Author(s) 2021